A novel approach to breast cancer diagnosis via PET imaging of microcalcifications using ^{18}F-NaF

George H. Wilson III[1], **John C. Gore**[1,2,3,4], **Thomas E. Yankeelov**[1,2,3,5], **Stephanie Barnes**[1,2], **Todd E. Peterson**[1,2], **Jarrod M. True**[1], **Sepideh Shokouhi**[1,2], **J. Oliver. McIntyre**[1,2,3,5], **Melinda Sanders**[6], **Vandana Abramson**[7], **The-Quyen Ngyuen**[3], **Anita Mahadevan-Jansen**[3], and **Mohammed N. Tantawy**[1,2]

[1]Vanderbilt University Institute of Imaging Science, Vanderbilt University Medical Center, Nashville, TN 37232, USA

[2]Department of Radiology and Radiological Sciences, Vanderbilt University Medical Center, Nashville, TN 37232, USA

[3]Biomedical Engineering, Vanderbilt University Medical Center, Nashville, TN 37232, USA

[4]Department of Molecular Physiology and Biophysics, Vanderbilt University Medical Center, Nashville, TN 37232, USA

[5]Cancer Biology, Vanderbilt University Medical Center, Nashville, TN 37232, USA

[6]Pathology, Vanderbilt University Medical Center, Nashville, TN 37232, USA

[7]Hematologu/Oncology, Vanderbilt University Medical Center, Nashville, TN 37232, USA

Abstract

Rationale—Current radiological methods for diagnosing breast cancer detect specific morphological features of solid tumors and/or any associated calcium deposits. These deposits originate from an early molecular microcalcification process which consists of two types: type 1 is calcium oxalate (CO) and type II is carbonated calcium hydroxyapetite (HAP). Type I microcalcifications are mainly associated with benign tumors while type II have been shown to be produced, internally, by malignant cells. No current non-invasive *in vivo* techniques are available for detecting intratumoral microcalcifications. Such a technique would have a significant impact on breast cancer diagnosis and prognosis in preclinical and clinical settings. ^{18}F-NaF PET has been solely used for bone imaging by targeting the bone HAP. In this work, we provide preliminary evidence that ^{18}F-NaF PET imaging can be used to detect breast cancer by targeting the HAP lattice within the tumor microenvironment with high specificity and soft-tissue contrast-to-background ratio, while delineating tumors from inflammation.

METHODS—Mice were injected with approximately 10^6 MDA-MB-231 cells subcutaneously and imaged with ^{18}F-NaF PET/CT in a 120 min dynamic sequence when the tumors reached a size of ~250 mm^3. Regions-of-interest (ROIs) were drawn around the tumor, muscle, and bone. The

Author to whom correspondence should be addressed: Mohammed N. Tantawy, Ph.D., 1161 21st Ave South, MCN AA-1105, Telephone number: 1(615) 343-4795, Fax number: 1(615) 322-0734, n.tantawy@vanderbilt.edu.
First author information: George H Wilson III, 1161 21st Ave South, MCN AA-1105, Telephone number: 1(615) 322-6639, Fax number: 1(615) 322-0734, george.h.wilson@vanderbilt.edu, Status: Student

concentration of the radiotracer within those ROIs were compared to one another. For comparison to inflammation, rats with inflammatory paws were subjected to ^{18}F-NaF PET imaging.

RESULTS—Tumor uptake of ^{18}F$^-$ was significantly higher (p<0.05) than muscle uptake where the tumor-to-muscle ratio was ~3.5. The presence of type II microcalcification in the MDA-MB-231 cell line was confirmed histologically using alizarin red S and von Kossa staining as well as Raman microspectroscopy. No uptake of ^{18}F$^-$ was observed in the rat inflamed tissue. Lack of HAP in the inflamed tissue was verified histologically.

CONCLUSIONS—This study provides preliminary evidence suggesting that specific targeting of the HAP within the tumor microenvironment with ^{18}F may be able to distinguishing between inflammation and cancer.

Keywords

Breast cancer; MDA-MB-231; microcalcification; ^{18}F-NaF; ^{18}F$^-$; PET; hydroxyapetite; calcium oxalate

Introduction

Breast cancer is the second most common malignancy among women, accounting for nearly one in three cancers diagnosed in the United States. It is the second leading cause of cancer death among women, causing almost 40,000 deaths in 2011 alone[1]. Current imaging techniques may fail to detect tumors (false negative) due to their small size or location in the breast, obscurity by nearby organs, or dense breast tissue[2].

One significant feature of breast cancer diagnosis is the presence of calcium deposits (average 0.3 mm^3 in size) detected *via* mammograms [3–5]. These calcium deposits are potentially the result of condensation of one of two types of microcalcification found within the tumor microenvironment: Type I which contains calcium oxalate dehydrate (CO), and Type II which contains calcium phosphates in the form of hydroxyapatite (HAP) [6]. Importantly, Type I deposits are associated with benign breast disease, while malignant cells have the unique capability to produce HAP[4, 7, 8]. Alkaline phosphatase (ALP) on the surface of malignant cells hydrolyses β-glycerophosphate (βG) to glycerol and inorganic phosphate (Pi), which is transported into the cell by the type II family of Na-Pi cotransporters. There, the Pi combines with calcium to produce HAP crystals. HAP then leaves the cells, by unknown mechanisms, into the extracellular matrix. Furthermore, HAP enhances the mitogenesis of mammary cells which amplifes the malignant process resulting in accelerated tumor growth[7, 8]. Therefore, HAP may be a biomarker for breast malignancy.

Apatite calcification in bone is generally composed of HAP[9]. The carbonate substitution for phosphate in the bioapatites significantly increases the reactivity of these compounds, especially to anions such as fluoride, allowing them to substitute into the lattice[10]. Sodium fluoride labeled with ^{18}F$^-$ (^{18}F-NaF) has previously been used for bone imaging and bone HAP abundance quantification, as well as for detecting bone metastases using positron emission tomography (PET). The free fluoride dissociates from the sodium and binds to the hydroxyapatite matrix ($Ca_{10}(PO_4)_6OH_2$) of the skeleton [11], where ^{18}F$^-$ substitutes for the OH$^-$ of the hydroxyapatite and forms fluoroapatite ($Ca_{10}(PO_4)_6F_2$)[12].

Our working hypothesis is that the same mechanisms of uptake of $^{18}F^-$ in bone apply to breast tumors containing HAP within their microenvironment. Therefore, we investigated the ability of ^{18}F-NaF to detect breast tumors *via* targeting the HAP microenvironment using mouse models of MDA-MB-231, a triple negative human breast cancer cell line that does not express the genes for estrogen receptor, progesterone receptor, or Her2/neu. MDA-MB-231 cells produce highly invasive malignant tumors[13]. Thus, this cell line is a prototype for highly differentiated breast cancer cells with overexpressed epidermal growth factor receptors[14]. We then assessed the ability of this technique to discriminate between inflammation and cancer by applying it to rat models of acute inflammation.

Methods

All studies were approved by the Vanderbilt University Animal Care and Use Committee prior to conducting the experiments.

Tumor model and imaging

MDA-MB-231 cells were cultured in Dulbecco's Modified Eagle's Medium (DMEM, Invitrogen, Carlsbad, CA) supplemented with 10% fetal bovine serum and 1% penicillin streptomycin (Invitrogen, Carlsbad, CA) at 37°C in a humidified, 5% CO_2 incubator. Four-to five-week old female Foxn1 nu/nu mice were injected subcutaneously in the right hind limb (n = 10) with ~10 million MDA-MB-231 cells in a 1:2 ratio of matrigel and DMEM.

Once the tumor size reached 200–400 mm^3, the mice were imaged in a microPET Focus 220 (Siemens Preclinical Solutions, Knoxville, TN) for 120 min in a dynamic acquisition mode with a simultaneous intravenous injection of ~18 Mbq ^{18}F-NaF, provided by the Vanderbilt radiochemistry core. All mice were anesthetized with 2% isofluorane vaporized with oxygen at a steady flow rate of 2.5 L/min during imaging. The dynamic acquisitions consisted of twelve 5 sec frames, four 60 sec frames, one 5 min frame, and eleven 10 min frames. All data sets were reconstructed using the MAP algorithm into 128 × 128 × 95 slices with a voxel size of 0.95 × 0.95 × 0.8 mm^3 at a beta value of 0.001. Immediately following the PET scans, the mice were imaged in a microCAT II (Siemens, Knoxville, TN) at X-ray beam intensity of 180 mAs and an X-ray tube voltage of 80 kVp for anatomical coregistration with the PET images. The images were reconstructed at 512 × 512 × 512 with a voxel size of 0.122 × 0.122 × 0.173 mm^3.

Inflammation model and imaging

Carrageenan (100 μL 1% in sterile saline) was injected subcutaneously in the rear right footpad of wild type Sprague Dally rats (n = 3). Two hours later, when inflammation was maximal[15], the rats were injected with ^{18}F-NaF and imaged in our microPET for 30 min at 1 hr post radiotracer administration in static mode followed by a CT scan as described earlier.

Histological search for hydroxyapetite

A-Staining—Immediately following PET/CT imaging, the tumors and muscle were harvested. For the rat inflammatory model, the feet were harvested at the end of the imaging session. Sections of the harvested tissue (5 μm) were loaded onto glass slides and assessed

for mineralization via alizarin red S and von Kossa staining. The staining process was carried out at the Vanderbilt Translational Pathology Shared Resource that uses manufacturer provided staining protocols. Positive staining for alizarin red S (color: red) indicates the presence of calcium while positive staining for von Kossa indicates the presence of calcium phosphates (color: black/brown)[8].

B-Raman microspectroscopy—The stained tissue sections, along with stained mouse bone sections provided by the Translational Pathology Core at Vanderbilt University, were subjected to Raman microspectroscopy using an inVia Raman Microscope (Renishaw, Gloucestershire, United Kingdom) using a 785 nm laser and a 50x objective (numerical aperture 0.75). Regions of 100×60 μm^2 of the sample were mapped over the entire section and Raman spectra were acquired over those areas with an axial resolution of 1 μm. A shift near 960 cm^{-1} is typical of HAP[6, 8, 16]. Spectra were processed using Renishaw-WiRE v3.3 software. The bone slides were used for initial calibration. Based on the Raman spectra, regions on the mapped sample were classified using a direct classical least squares method and were color-coded in green indicating a 960 cm^{-1} shift or black (no shift).

Data analysis

Anatomical regions-of-interest (ROIs) were drawn around the entire tumor, hip bones, lungs, heart, pineal gland, and muscle of the opposing hind limb in the CT images (except for the pineal gland) for each mouse using the medical imaging analysis tool AMIDE[17] and superimposed on the PET images. The pineal gland ROI was directly drawn on the PET image as the CT image cannot accurately distinguish brain regions. Time-activity curves (TACs) were established for all ROIs over the entire duration of the dynamic scans. For the rat inflammation studies, ROIs were drawn around each of the paws of the rats in the CT image and superimposed on the PET images.

The initial distribution of $^{18}F^-$ is determined by blood flow, after which most of it is cleared rapidly from plasma and excreted by the kidneys[12]. In the bone, the $^{18}F^-$ ions pass through plasma to the extracellular fluid space, into the shell of bound water onto the hydroxyapatite crystal surface, and into the interior of the crystal, where $^{18}F^-$ exchanges for OH^- on the HAP lattice. The kinetics of $^{18}F^-$ moving from the blood plasma to incorporation into fluoroapatite ($Ca_{10}(PO_4)_6F_2$) have been described by a three compartment model[12, 18] as demonstrated in Figure 1. Therefore, we used a similar model to describe tumor uptake of $^{18}F^-$.

The mean concentrations of $^{18}F^-$ within a 20 min time interval between 40 and 60 min post ^{18}F-NaF injection were normalized to the total injected dose (%ID/cc) for the tumor, muscle, and bone regions of the mice. This time window was chosen based on the results we obtained as demonstrated in the results section below. Similarly, the %ID/cc for the rat paws was measured for the entire scan (30 min). A two-tailed Student t-test was used to compare %ID/cc between the tumor and muscle, and between tumor and bone in the mice; the statistical significance threshold was considered to be p<0.05.

Results

Initial perfusion of $^{18}F^-$ was observed in all tissues, including tumor and muscle, within the first minute following injection of ^{18}F-NaF. The $^{18}F^-$ ions were quickly excreted by the kidneys and by ~ 40 min, residual ions were concentrated in the bone and tumor with little or no signal observed in the muscle as shown in Figure 2. The TACs were fairly flat from 40–120 min indicating a state of equilibrium as demonstrated in Figure 3. Washout of the radiotracer from bone and tumor was fairly slow as indicated by a negligible k_4 (please see Table 1). Therefore, we measured the $^{18}F^-$ uptake constant as $K_{18F} = K_1k_3/(k_2+k_3)$.

The concentration of $^{18}F^-$ in the tumor between 60 and 80 min was ~3.5 times higher than that of muscle (n = 7, p<0.05) where the %ID/cc within the tumor ROI was 2.9 ± 0.8 (mean $\pm$ SD) and that of muscle and bone %ID/cc were 0.8 ± 0.2, and 31 ± 4, respectively.

Positive staining for calcium (red; alizarin red S) and calcium phosphate (black/brown; von Kossa) were observed in both the tumor and bone, as shown in Figure 4. The positive stain for von Kossa suggests the presence of Type II calcifications specifically[8]. A Raman shift of ~960 cm^{-1} was observed for the MDA-MB-231 slides as shown in Figure 4 where the green color in the 100×60 μm^2 Raman image taken over the tumor section indicates everywhere a shift near 960 cm^{-1} was found within that region. Thus, we confirmed the presence of carbonated calcium hydroxyapetite, type II microcalcifications, in the MDA-MB-231 microenvironment. No positive staining using alizarin red S or von Kossa was observed for the muscle, nor did we observe a HAP Raman shift in these tissue.

In some cases, we observed a localized region that had a very high concentration of $^{18}F^-$ (approximately nine times higher than muscle, %ID/cc > 8.5, n = 3) as shown in Figure 5. Interestingly, these mice were also the only mice with tumors that had started to ulcerate. In addition, no solid calcium deposits were observed in the CT scans. These mice were excluded from the statistical analysis since their %ID/cc were more than twice the standard deviation from the mean (physiologically, the skin surrounding the tumor was red in appearance indicating the initial stages of ulceration). Autoradiography correlated well with the von Kossa stain results as shown in Figure 5.

We did not observe any $^{18}F^-$ uptake, nor positive staining for Alizarin red S or von Kossa, in the inflamed soft tissue of the rat paws as shown in Figure 6; for comparison, %ID/cc of non-inflamed soft-tissue and paw bone were 0.9 ± 0.4 and 29 ± 3, respectively. As expected, no Raman shift at ~960 cm^{-1} was detected in the inflamed tissue, indicating the lack of HAP in them (data not shown as the Raman images appear as just black rectangles).

Accumulation of $^{18}F^-$ was also observed in the corpora arenacea (brain sand) known to contain hydroxyapetite in humans and animals[19–21] as shown in Figure 2.

Discussion

This study presents the first proposed use of ^{18}F-NaF PET imaging to specifically detect tumors based on their HAP abundance. The $^{18}F^-$ concentration was approximately 10 times higher in the bone compared to the tumors, which is expected due to the large density of

HAP in the bone and the large bone surface area. This is also indicated by the higher $^{18}F^-$ uptake in the bone illustrated by K_{18F} (please see Table 1). Therefore, in order to visually identify the tumor in the PET images, the windowing level was adjusted to a maximum of 12 % ID/cc as shown in Figure 2, causing the bone signal to appear saturated. For bone structure identification, the high end of the scale bar would be set to at least 45% so that the tumor is not be visible. In addition, the minimum windowing level was set to 0.8 % ID/cc to mask out normal tissue perfusion (e.g., muscle). All analysis of PET images in this work used these same windowing limits.

We are not aware of any negative control tumor models due to the limited studies carried out on HAP and breast cancer. As some breast lesions may be inflammatory lesions, we used an inflammatory rodent model to study the ability of $^{18}F^-$ PET images to distinguish between inflammation and malignancy. No accumulation of $^{18}F^-$ occurred in the rat inflammatory tissue due to lack of HAP (please see Figure 6). Therefore, this technique may indeed represent a novel and potentially reliable noninvasive *in vivo* method for distinguishing between malignant and inflammatory lesions with high specificity or between lesions that contain HAP and those that don't. This capability has not been shown in other imaging modalities and techniques. In addition, this technique can be used to measure HAP abundance and the relationship between tumor progression and HAP in preclinical settings.

The lack of accumulation of $^{18}F^-$ in the normal soft tissue, taken with the accumulation of $^{18}F^-$ in the brain sand and the tumor, supports the specificity of $^{18}F^-$ in binding to HAP when present in soft tissue. This occurs through mechanisms similar to those of bone uptake of $^{18}F^-$, with high soft tissue contrast-to-background ratio as no accumulation of the tracer occurs in soft tissue not containing HAP.

Calcium oxalate is implicated in the composition of most kidney stones[22–25]. It has been shown that prolonged exposure to high concentrations of NaF (60 mM) was able to dissolve CO in vitro, but this concentration would be considered toxic *in vivo* [26]. Since radiotracer concentrations, including ^{18}F-NaF, are on the order of sub-micromolars or smaller [27], it is highly unlikely that ^{18}F-NaF can break the calcium oxalate bond in benign breast lesions. Therefore, this technique can be used to not only detect single and multicentric tumors with high contrast-to-background ratio, but also to differentiate between type I and type II microcalcifications within the tumor's microenvironment.

This imaging technique can be rapidly translated to clinical trials since ^{18}F-NaF, or $^{18}F^-$, is already FDA approved. While the approach is not appropriate for screening, it could be deployed to support mammograms where suspicious lesions or multicentric lesions are detected and biopsy is not feasible. The total-body adsorbed dose is about 0.024 mSv/MBq (0.989 mrem/mCi) or 4.44 mSv for a typical 185 MBq (5 mCi) dose of ^{18}F-NaF injection which is well within the radiation dose tolerance for non-radiation workers[28]. Additionally, as microcalcifications were detected with ^{18}F-NaF PET imaging when no solid calcium deposits were observed in the CT scan, this technique could be useful in early breast cancer diagnosis before solid calcium deposits are visible in mammograms. This is especially important in cases of chronic inflammation, ductal carcinoma *in situ* (DCIS), or lobular carcinoma *in situ* (LCIS), which could progress to malignancy over time [29–31].

It is worth noting that there have been previous studies that used $^{18}F^-$ and sometimes a cocktail of $^{18}F^-$ and ^{18}F-FDG in breast cancer studies [32, 33]. Those studies, however, focused on bone metastases of breast cancer, and the patients imaged were at an advanced stage where the cancer had already spread and metastasized at different locations of the skeleton. Our work suggests the use of $^{18}F^-$ imaging within the breast and at a very early stage for means of primary detection, rather than metastases detection.

Conclusion

The results from this study provide the first evidence that PET imaging of breast cancer with $^{18}F^-$ via specifically targeting HAP within the tumor microenvironment may be able to provide a sensitive and non-invasive identification of intra-tumoral microcalcifications with high specificity and contrast-to-background ratio, as this technique targets type II microcalcifications *in vivo*. Due to radiation and cost, this technique could not be used for initial screening for breast cancer. However, it can be used in identifying multicentric tumors, as well as in discriminating between malignancies and benign factors (e.g. inflammation, cysts, and fat necrosis). Additionally, this technique can be used in the early detection of breast cancer cells progressing from chronic inflammation, DCIS, or LCIS, avoiding repeated biopsies.

Acknowledgments

References

1. DeSantis C, Siegel R, Bandi P, Jemal A. Breast cancer statistics, 2011. CA: a cancer journal for clinicians. Nov-Dec;2011 61(6):409–418. [PubMed: 21969133]

2. Agency for health care research and quality. Comparative Effectiveness of Non-Invasive Diagnostic Tests for Breast Abnormalities – An Update of a 2006 Report. Effective Health Care Program: Research Review. 2012 Feb.

3. Gershon-Cohen J. The importance of x-ray microcalcifications in breast cancer. The American journal of roentgenology, radium therapy, and nuclear medicine. Apr; 1967 99(4):1010–1011.

4. Baker R, Rogers KD, Shepard N, Stone N. New relationships between breast microcalcifications and cancer. BrJ Cancer. 2010; 103(7):1034–1039. [PubMed: 20842116]

5. Going JJ, Anderson TJ, Crocker PR, Levison DA. Weddellite calcification in the breast: eighteen cases with implications for breast cancer screening. Histopathology. Feb; 1990 16(2):119–124. [PubMed: 2323732]

6. Haka AS, Shafer-Peltier KE, Fitzmaurice M, Crowe J, Dasari RR, Feld MS. Identifying microcalcifications in benign and malignant breast lesions by probing differences in their chemical composition using Raman spectroscopy. Cancer research. Sep 15; 2002 62(18):5375–5380. [PubMed: 12235010]

7. Morgan MP, Cooke MM, Christopherson PA, Westfall PR, McCarthy GM. Calcium hydroxyapatite promotes mitogenesis and matrix metalloproteinase expression in human breast cancer cell lines. Molecular carcinogenesis. Nov; 2001 32(3):111–117. [PubMed: 11746823]

8. Cox RF, Hernandez-Santana A, Ramdass S, McMahon G, Harmey JH, Morgan MP. Microcalcifications in breast cancer: novel insights into the molecular mechanism and functional consequence of mammary mineralisation. Br J Cancer. 2012; 106(3):525–537. [PubMed: 22233923]

9. Pleshko N, Boskey A, Mendelsohn R. Novel infrared spectroscopic method for the determination of crystallinity of hydroxyapatite minerals. Biophysical journal. Oct; 1991 60(4):786–793. [PubMed: 1660314]

10. Nelson DG. The influence of carbonate on the atomic structure and reactivity of hydroxyapatite. Journal of dental research. Aug; 1981 60(Spec No C):1621–1629. [PubMed: 6943172]

11. Hawkins RA, Hoh C, Glaspy J, et al. The role of positron emission tomography in oncology and other whole-body applications. Seminars in nuclear medicine. Oct; 1992 22(4):268–284. [PubMed: 1439872]

12. Czernin J, Satyamurthy N, Schiepers C. Molecular Mechanisms of Bone 18F-NaF Deposition. Journal of Nuclear Medicine. Dec 1; 2010 51(12):1826–1829. [PubMed: 21078790]

13. Korah RM, Sysounthone V, Golowa Y, Wieder R. Basic fibroblast growth factor confers a less malignant phenotype in MDA-MB–231 human breast cancer cells. Cancer research. Feb 1; 2000 60(3):733–740. [PubMed: 10676661]

14. Aboagye EO, Bhujwalla ZM. Malignant Transformation Alters Membrane Choline Phospholipid Metabolism of Human Mammary Epithelial Cells. Cancer research. Jan 1; 1999 59(1):80–84. [PubMed: 9892190]

15. Uddin MJ, Crews BC, Ghebreselasie K, et al. Fluorinated COX–2 inhibitors as agents in PET imaging of inflammation and cancer. Cancer prevention research. Oct; 2011 4(10):1536–1545. [PubMed: 21900596]

16. Nelson DG, Featherstone JD. Preparation, analysis, and characterization of carbonated apatites. Calcified tissue international. 1982; 34(Suppl 2):S69–81. [PubMed: 6293677]

17. Loening AM, Gambhir SS. AMIDE: a free software tool for multimodality medical image analysis. Mol Imaging. 2003; 2(3):131–137. [PubMed: 14649056]

18. Blau M, Ganatra R, Bender MA. 18 F-fluoride for bone imaging. Seminars in nuclear medicine. Jan; 1972 2(1):31–37. [PubMed: 5059349]

19. Schmid HA, Requintina PJ, Oxenkrug GF, Sturner W. Calcium, calcification, and melatonin biosynthesis in the human pineal gland: a postmortem study into age-related factors. Journal of pineal research. May; 1994 16(4):178–183. [PubMed: 7807371]

20. Krstic R, Golaz J. Ultrastructural and X-ray microprobe comparison of gerbil and human pineal acervuli. Experientia. Apr 15; 1977 33(4):507–508. [PubMed: 862751]

21. Alcolado JC, Moore IE, Weller RO. Calcification in the human choroid plexus, meningiomas and pineal gland. Neuropathology and applied neurobiology. May-Jun;1986 12(3):235–250. [PubMed: 3736772]

22. Coe FL, Parks JH, Asplin JR. The pathogenesis and treatment of kidney stones. The New England journal of medicine. Oct 15; 1992 327(16):1141–1152. [PubMed: 1528210]

23. Lemann J Jr. Composition of the diet and calcium kidney stones. The New England journal of medicine. Mar 25; 1993 328(12):880–882. [PubMed: 8441433]

24. Parmar MS. Kidney stones. Bmj. Jun 12; 2004 328(7453):1420–1424. [PubMed: 15191979]

25. Moe OW. Kidney stones: pathophysiology and medical management. Lancet. Jan 28; 2006 367(9507):333–344. [PubMed: 16443041]

26. Low RK, Ho S, Stoller ML. Sodium fluoride dissolution of human calcium oxalate/phosphate stone particles. Journal of endourology / Endourological Society. Oct; 1995 9(5):379–382. [PubMed: 8580936]

27. Cook GJ. Oncological molecular imaging: nuclear medicine techniques. The British journal of radiology. 2003; 76(Spec No 2):S152–158. [PubMed: 15572337]

28. Segall G, Delbeke D, Stabin MG, et al. SNM practice guideline for sodium 18F-fluoride PET/CT bone scans 1.0. J Nucl Med. Nov; 2010 51(11):1813–1820. [PubMed: 21051652]

29. Wiechmann L, Kuerer HM. The molecular journey from ductal carcinoma in situ to invasive breast cancer. Cancer. May 15; 2008 112(10):2130–2142. [PubMed: 18383519]

30. Moran M, Haffty BG. Lobular carcinoma in situ as a component of breast cancer: the long-term outcome in patients treated with breast-conservation therapy. International journal of radiation oncology, biology, physics. Jan 15; 1998 40(2):353–358.

31. Aulmann S, Penzel R, Schirmacher P, Sinn HP. Lobular carcinoma in situ (LCIS): risk factor and precursor of invasive lobular breast cancer. Verhandlungen der Deutschen Gesellschaft fur Pathologie. 2007; 91:208–213. [PubMed: 18314616]

32. Iagaru A, Mittra E, Yaghoubi SS, et al. Novel strategy for a cocktail 18F-fluoride and 18F-FDG PET/CT scan for evaluation of malignancy: results of the pilot-phase study. J Nucl Med. Apr; 2009 50(4):501–505. [PubMed: 19289439]

33. Doot RK, Muzi M, Peterson LM, et al. Kinetic analysis of 18F-fluoride PET images of breast cancer bone metastases. J Nucl Med. Apr; 2010 51(4):521–527. [PubMed: 20237040]
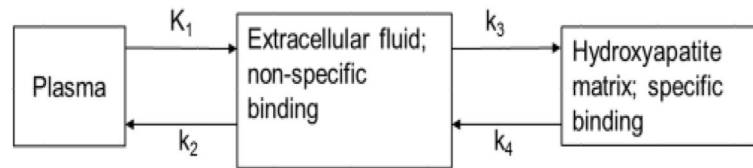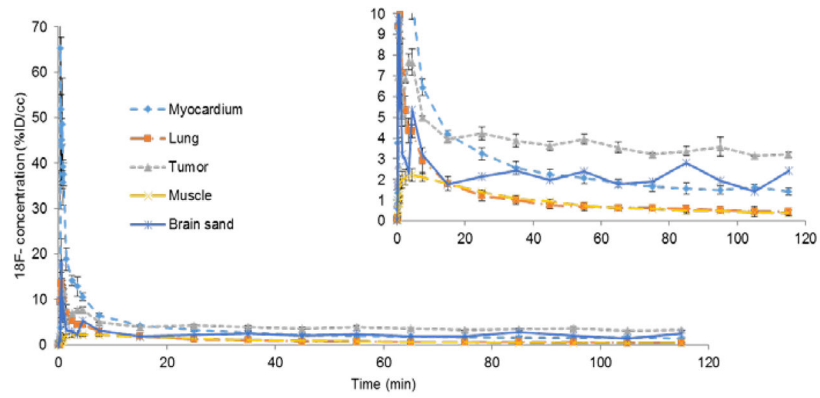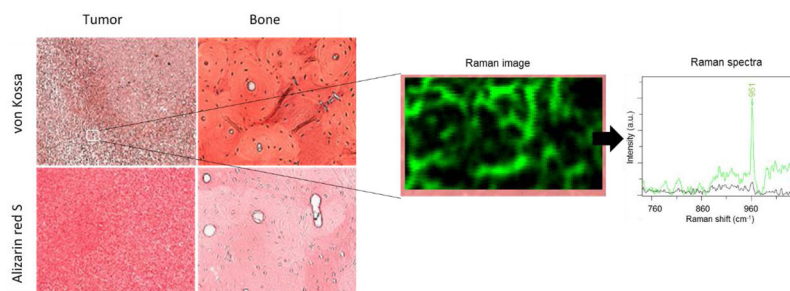
Figure 1.
A three compartment model was used to describe the kinetic distribution of $^{18}F^-$ ions to tumor and bone. K_1 is the transfer rate of $^{18}F^-$ from the first compartment 1 (plasma) to compartment 2 (extracellular fluid space) in units of mL/min/g, k_2 is the transfer rate from 2 to 1 (1/min), k_3 is the transfer rate from 2 to compartment 3 (hydroxyapatite lattice) in units of 1/min, and k_4 is the transfer rate. from 3 to 2 (1/min).
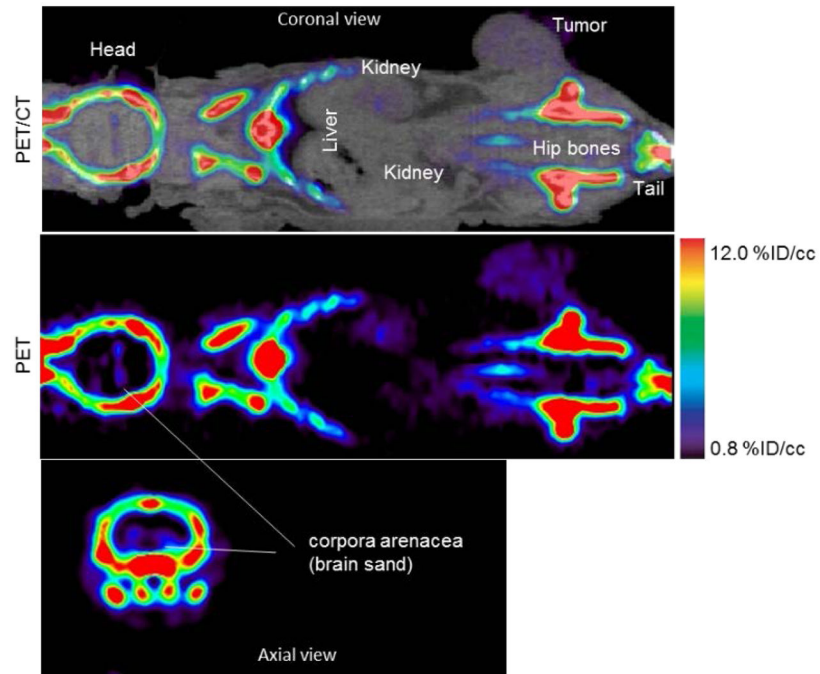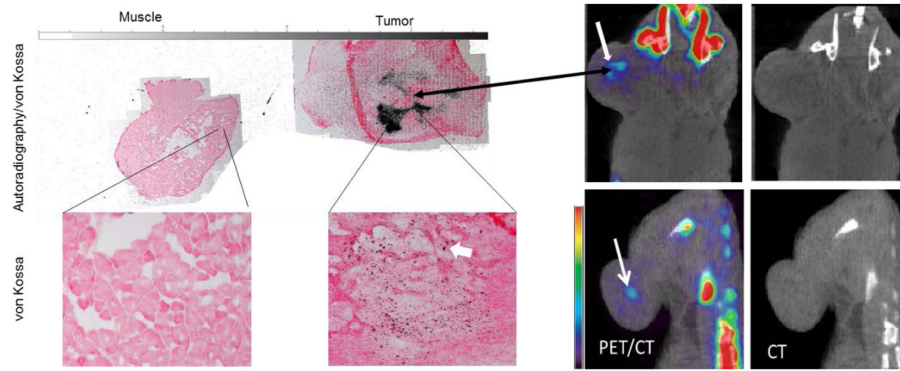
Figure 2.
A 60–80 min summed PET/CT and PET images of $^{18}F^-$ uptake in a mouse bearing MDA-MB-231 tumor and imaged for 120 min. With the windowing level set between 0.8 and 12% ID/cc, bone image is saturated but the tumor and brain sand are visible with high contrast-to-background soft-tissue ratio

Figure 3.
Time-activity curves (TACs) of different regions in the mouse injected with ^{18}F-NaF displayed in the previous figure. The percent injected dose per unit volume (%ID/cc) is the ^{18}F$^-$ concentration within each ROI normalized to the total injected dose. The insert is just a zoomed view of the TACs.
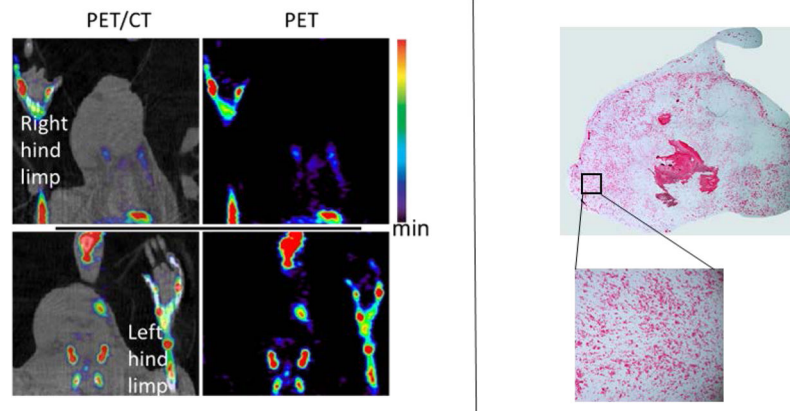
Figure 4.
Staining of MDA-MB-231 breast cancer samples and normal bone. With von Kossa (red/brown) and alizarin red S (red). The positive von Kossa stains indicate the presence of calcium carbonates suggesting the presence of Type II calcification specifically. A 100×60 μm^2 region of the same tumor section scanned with a Raman microscope revelas the locations within that region where a 960 cm^{-1} shift was found (green color in the Raman image and Raman spectra) and where no shift near 960 cm^{-1} (black color). A shift at ~960 cm^{-1} indicates the presence of HAP.

Figure 5.
A coronal view of a PET/CT and CT only images of two mice injected with ^{18}F-NaF (right) and the corresponding autoradiography/von Kossa staining of a tumor section and normal muscle (left). A localized region, indicated by the thick white arrow, with high ^{18}F$^-$ (about 9 times higher than muscle and 3 times less than bone) was observed in each tumor in the PET images indicating dense HAP. These regions was not observed in the CT images. The autoradiography correlated well with the PET and staining results.

Figure 6.
(Left) A rat model of acute inflammation (in right footpad) imaged with 18F- NaF PET at maximal inflammation. Uptake of $^{18}F^-$ was limited to bone with no accumulation in the inflammatory soft tissue due to lack of HAP. (Right) A section of the inflamed tissue stained with von Kossa. No positive staining (nor red/brown spots) was observed within in the stained tissue indicating no presence of calcium phosphates or type II microcalcification. The lower and upper limits scale bar are 0.8 and 12 %ID/cc.

Table 1

Kinetic parameters of $^{18}F^-$ uptake in mice bearing MDA-MB-231 tumors. The tumors contain hydroxyapetite similar to what is found in normal bone. All value are presented as mean ± SD. K_{18F} is the $^{18}F^-$ uptake constant described as $K_1 k_2/(k_2+k_3)$.

Region	K_1 (ml/g/min)	k_2 (1/min)	k_3 (1/min)	k_4 (1/min)	K_{18F} (ml/g/min)
Tumor	0.42 ± 0.19	1.27 ± 0.92	0.07 ± 0.06	0.03 ± 0.02	0.03 ± 0.01
Bone	0.25 ± 0.11	0.44 ± 0.12	0.60 ± 0.42	0.002 ± 0.002	0.14 ± 0.08